Chapter 3
Gas–Electron Interaction in the ETEM

Jakob B. Wagner and Marco Beleggia

Abstract Imaging in a differential pumped environmental TEM (ETEM) results in general in a degradation of the image quality. Scattering of electrons by gas molecules in the pressurized volume between the pole pieces blurs the image and decreases the signal-to-noise ratio of the acquired images. The somewhat simple picture of a plane wave interacting with the sample of interest is no longer valid. Furthermore, the exit wave from the sample is altered by scattering events taking place after the sample in the direction of propagation. In this chapter, the effect of the increased gas pressure between the pole pieces in an aberration-corrected high-resolution transmission electron microscope is discussed in order to shine some light on the additional phenomena occurring in ETEM compared to conventional HRTEM. Both direct effects on the image quality and more indirect effects rising from gas ionization are discussed.

3.1 Introduction

Ever since the proposal and first attempts of in situ electron microscopy involving non-vacuum imaging in the early days of electron microscopy (see Chap. 1) addressing the influence of the gas on the fast electron pathway has been crucial. The higher the pressure and the longer gas path the fast electrons have to pass, the larger is the probability of scattering events between electrons and gas species.

J.B. Wagner (✉)
Center for Electron Nanoscopy, Technical University of Denmark, Kgs. Lyngby, Denmark
e-mail: jakob.wagner@cen.dtu.dk

M. Beleggia
Center for Electron Nanoscopy, Technical University of Denmark, Kgs. Lyngby, Denmark

Helmholtz-Zentrum Berlin for Materials and Energy, Berlin, Germany

T.W. Hansen, J.B. Wagner (eds.), *Controlled Atmosphere Transmission Electron Microscopy*, DOI 10.1007/978-3-319-22988-1_3

The scattering on gas molecules results in a significant loss of electrons (intensity) on the viewing screen depending on the gas species, total pressure and energy of the primary electrons. Furthermore, the spatial resolution will decrease both for scanning transmission electron microscopy (STEM) and for broad beam electron microscopy. The contrast in the resulting images might be influenced as well depending on the scattering power of the gas molecules.

Not only the spatial resolution and contrast of the acquired micrographs will be affected by the electron–gas interaction, but the observations will also be influenced indirectly by ionization of gas species, which can lead to more reactive gas species and charge transfer effects. For example, the ionized gas species can be used for charge compensation since ionized gas species act as charge carriers compensating for charging of the sample during electron beam irradiation.

The effect on the special resolution might be easier to understand qualitatively in the case of scanning transmission electron microscopy. The highly focussed beam gets more diffuse on the sample as the fast electron scatters on gas species above the specimen. This beam broadening effect has been studied in great detail in the SEM community for decades (Danilatos 1988; Belkorissat et al. 2004; Mansour et al. 2009, 2013; Danilatos et al. 2011). However, the understanding of the effects on intensity, resolution, and (phase) contrast for broad beam electron microscopy is still in its infancy, and it is the focus of the present chapter.

In TEM where the spatial resolution relies on the coherency of the fast electron beam, the scattering effects taking place both above and below the sample strongly influence the resolution and signal to noise. Figure 3.1 illustrates the reduction of a cobalt oxide surface layer embedding a Co nanoparticles supported on α-Al_2O_3. The striking difference between the two images is the removal of the oxide layer. However, the signal-to-noise of the image in general is decreased when imaging in 740 Pa of CO (used as reducing agent). The insets in Fig. 3.1c, d clearly show that the high spatial frequency information is damped in the presence of CO in the microscope.

Obviously the effect of the gas species is related to the amount of gas present in the electron path (pressure of gas), but also the electron-optical conditions such as total beam current, current density, and primary beam energy have been found to influence the image quality to a greater extent when imaging in the presence of gas compared to traditional imaging in vacuum. In order to understand these direct effects on the image quality or instrument performance the geometry of the instrument and the scattering events taking place during the electron beam passage of the high-pressure volume have to be described in detail. In the present chapter effects of electron gas scattering is described and discussed to elucidate some of the aspects, which have to be considered in differential pumped environmental microscopy.

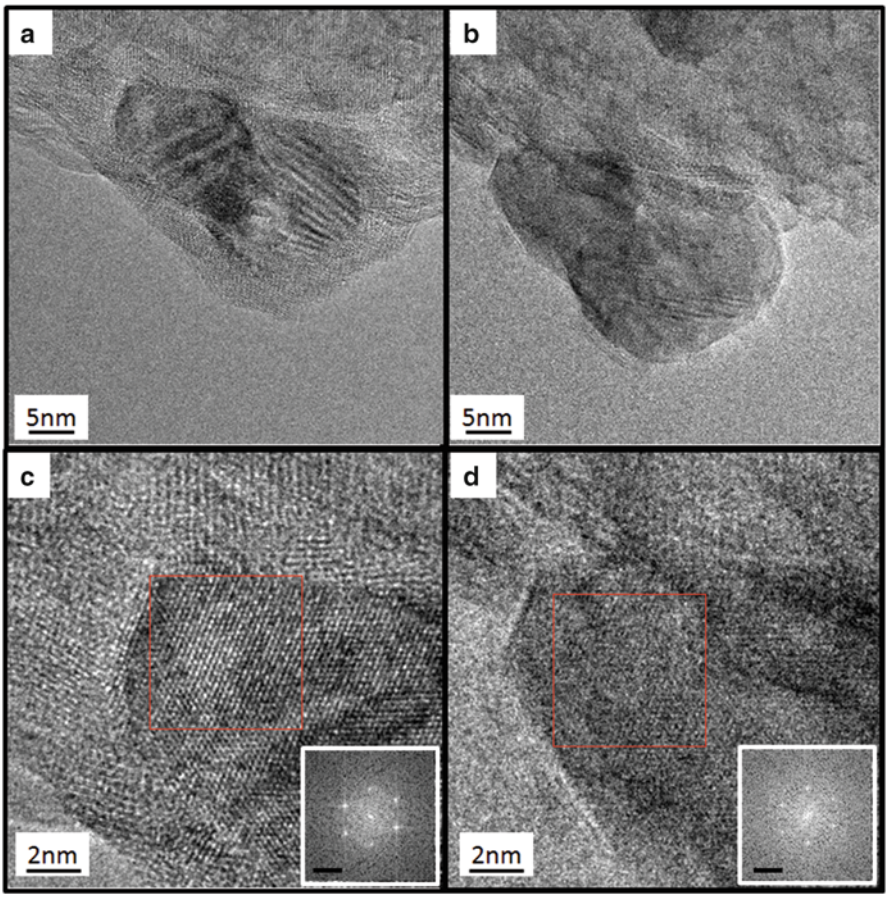

Fig. 3.1 Co/α-Al_2O_3 imaged in (**a**) high vacuum and (**b**) in the presence of 740 Pa of CO at 250 °C. (**c**, **d**) Close-up and FFT of marked areas in vacuum and presence of CO, respectively. The interaction of the fast electrons with the gas molecules decrease the resolution and signal to noise of the final image. Acquisition time and optical parameters of the electron microscope are the same for the two images

3.2 Influence on Instrument Performance

3.2.1 Geometric Considerations

The effect of the scattering of the swift electron on gaseous molecules near the sample of interest on the image quality and information transferred to the imaging system is dependent on the exact geometry of the high-pressure volume surrounding the sample.

As described in detail in dedicated chapters in the present book two main paths are pursued in order to allow controlled atmosphere around the sample:

(1) The windowed cell, which encapsulate the high-pressure gas around the sample by electron transparent windows and (2) the differential pumped version where a direct line of sight is available and the pressure is confined by pressure-limiting apertures.

Whereas the windowed cell usually limits the high-pressure volume to a thickness less than 50 μm in the direction of the propagating electron beam, the differentially pumped version have the high-pressure zone confined in the full volume between the pole pieces—the typical distance between the pressure-limiting apertures in commercially available ETEMs is in the order of 5–7 mm.

As described above, electrons should traverse the shortest possible path through gas in order to minimize the artefacts due to scattering of electrons on gas molecules. This is accomplished in the windowed cell, but on the expense of having two solid membranes interacting with the swift electrons as well disturbing the wave function. Thinner membranes are constantly developed in order to minimize this artefact maintaining the strength to withstand the pressure difference as further described in Chap. 6. The effect of the membranes on the spatial resolution has been studied in detail by Yaguchi et al. (2011), who, not surprisingly, found that 200 nm Si_3N_4 membranes cause a more significant loss in spatial resolution of the final image compared to the use of 15 nm Si_3N_4 membranes for the windowed cell. With membranes designed specifically to minimize their bulging during high pressure while maintaining a relatively large field of view, lattice fringe images can be recorded at pressures of more than 100 kPa (Creemer et al. 2008; Vendelbo et al. 2013, 2014). In this case the pathway of the fast electrons through the high-pressure zone is limited to around 50 μm.

Comparing the pathway of the high energetic electrons through the high-pressure zone in a differential pumped environmental TEM such as the aberration corrected FEI Titan 80-300 ETEM gives an indication of the pressure resulting in a similar amount of scattering event as described above. The high-pressure zone is confined by the pressure-limiting apertures placed at the pole pieces resulting in a pathway of around 7 mm (Hansen et al. 2010). The pathway is around two orders of magnitude longer in the aperture-limiting setup compared to the windowed solution. The upper limit of pressure allowing lattice fringe imaging is around two orders of magnitude lower for the aperture-limiting setup. Virtually compressing a 7 mm slab of gas at 1 kPa into the same atomic density as a solid results in a "solid" of around 10 nm in thickness—a typical value that allows for good lattice fringe imaging conditions. However, the scattering on gas molecules takes place over the full pathway between the pole pieces and not only in the intended object plane for conventional samples. The extended volume of scattering events includes the front focal and back focal plane as indicated in Fig. 3.2. This implies that the scattering geometry of the electron–gas interaction has to be revised. The rather complex trajectories which the scattered electron now follows lead to a loss of intensity in the final image as electrons being scattered above and below the sample are captured by apertures (or the column itself). In the windowed cell approach, the electron–gas scattering takes place closer to the intended objective plane and the conventional tracing of scattering event is more suitable in this case.

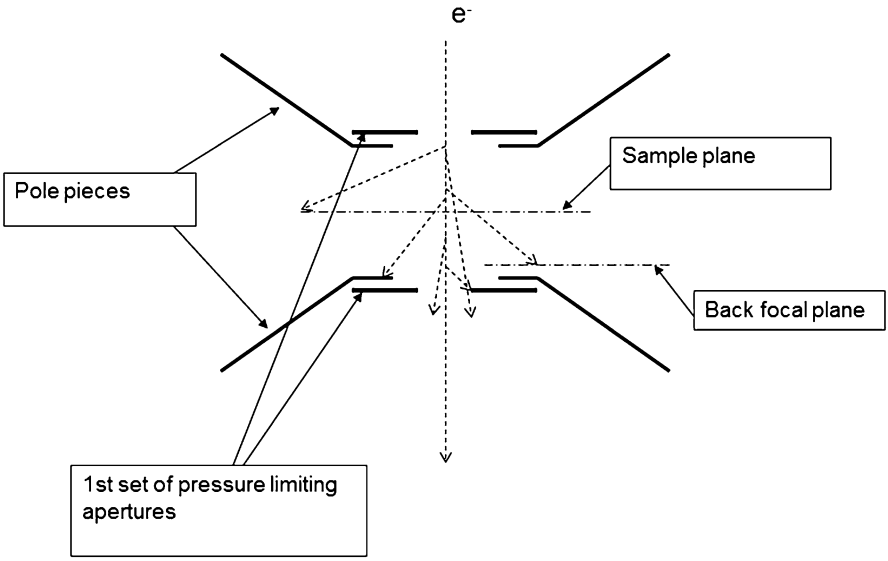

Fig. 3.2 Scattering of electrons on gas molecules in a differential pumped ETEM. (**a**) Scattering of electrons on gas molecules (indicated by *hatched lines*) takes place mainly between the first set of pressure-limiting apertures, which extend the focal length of the objective lens. The effect of the objective lens on the electron "trajectories" is not included in this drawing. The sketch is not to scale. Modified from Wagner et al. (2012)

3.2.2 Loss of Intensity

One of the immediate observed effects of letting gas into the microscope is the significant loss of intensity in the image. Measuring the intensity by summing the counts on the CCD at a given magnification and optical configuration as a function of gas pressure, gas composition, and acceleration voltage reveals that the intensity can be reduced as much as 95 % within the pressure range compatible with the differentially pumped ETEM. Figure 3.3 shows the normalized CCD count (count per pixel) in the absence of a solid sample. The intensity is normalized with respect to the measured intensity in traditional high vacuum mode ($P = 10^{-4}$ Pa). The measurements are plotted as function of pressure in different gases (H_2, He, N_2, O_2, and Ar). The gases represent a range of molecular mass typically for the gases used in the ETEM. The measurements are performed at three different acceleration voltages of the microscope as well. It is obvious that the measured intensity at the CCD in general is decreasing with increasing gas pressure. The density of gas molecules in the path of the electron beam increases with increasing pressure and thereby increases the probability of an electron–gas scattering event resulting in the electron being stopped by apertures in the microscope column.

The cross section of scattering events between fast electrons and molecules depends on the energy of the swift electrons: the higher the energy the lower the

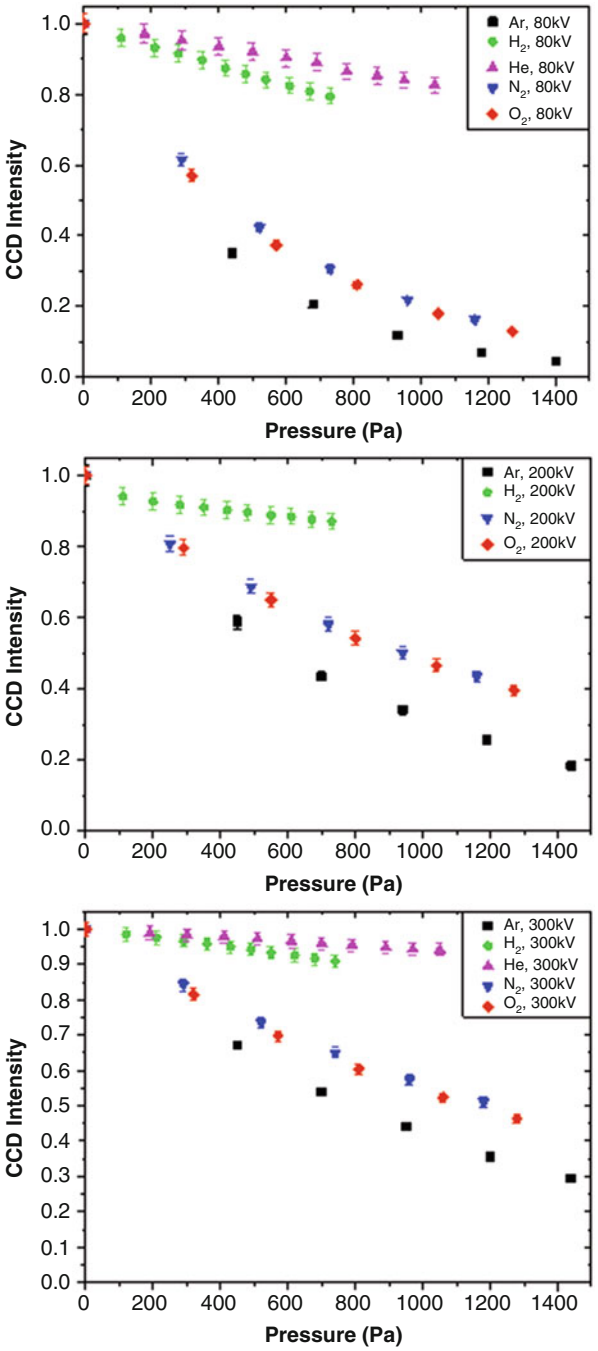

Fig. 3.3 The effect of the primary electron beam scattering on gas molecules in a differentially pumped environmental TEM. Normalized image intensity (without a specimen present) measured on a pre-GIF Ultrascan CCD camera, plotted as a function of gas pressure for various gas molecules at 80, 200, and 300 kV. The significant loss of intensity (counts) at the camera results in general in lower signal-to-noise ratio of the acquired images

cross section, as the electrons have less time to interact with the molecules along their path, decreasing the probability of interaction. Figure 3.3 shows clearly that the loss of intensity is, in general, larger for experiments performed at lower acceleration voltage of the primary electron beam in the presence of gas.

The measured intensity of the electron beam varies also with the atomic number of the gas species. Whereas the measured intensity only varies little for lighter molecules such as hydrogen and helium, the recorded intensity is less than 30 % of the vacuum value in 1400 Pa of argon using 300 kV primary electrons. With 80 kV electrons, the remaining intensity is less than 10 %. These observations indicate that the scattering cross section needs to be taken into account when estimating the loss of intensity for a TEM experiment. The scattering of electrons by gas molecules follows the atomic number.

Both the elastically and inelastically scattered electrons are contributing to the measured intensity. Electron energy-loss spectroscopy (EELS) reveals both low-loss and core-loss features corresponding to ionization of the gas molecules present between the pole pieces. As the pressure in the objective lens is increased, the ratio between the low-loss features and the zero-loss peak increases as expected. The fraction of the total intensity of the inelastically scattered electrons is indicative of the gas pressure in the pole piece gap.

The same trend in loss of intensity for the differentially pumped pathway of having gas in the microscope has been reported by Jinschek and Helveg (2012) for N_2 in a ETEM operated at 300 kV at different pressures. As a result of the decreased intensity the signal-to-noise ratio is also decreased with increasing gas pressure between the pole pieces. This will of course influence the image quality and thereby the spatial resolution obtainable from images at a given electron dose. Compensating by increasing the total dose during imaging will not always be a valid opportunity as both sample drift and beam damage might influence the observations as discussed below.

One way to minimize the loss of intensity in the acquired images is to decrease the total probability of electron–gas scattering at a given pressure by decreasing the gas path length. Decreasing the gas path length by encapsulating the high-pressure gas zone between impermeable membranes allows for higher pressures without losing too much intensity. Calculations by Yaguchi et al. show that the amount of unscattered 300 kV electrons is reduced by 70 % in 1×10^5 Pa of air having a 0.5 mm gas path length (Yaguchi et al. 2011). Comparing to the measured values in Fig. 3.3 it is found that a similar intensity loss is found for approximately 800 Pa gas (O_2–N_2) in a pole piece gap of 7 mm. The projected density of gas molecules is comparable in the two cases. Advantages and disadvantages of the membrane solution for high-pressure TEM measurements are addressed in more detail in Chap. 6.

3.2.3 Resolution in TEM

Besides the loss of intensity of the acquired images when having gas species in the microscope, the spatial resolution in general decreases with increasing gas pressure. To explore the effects of gas–electron interaction on the degradation of spatial

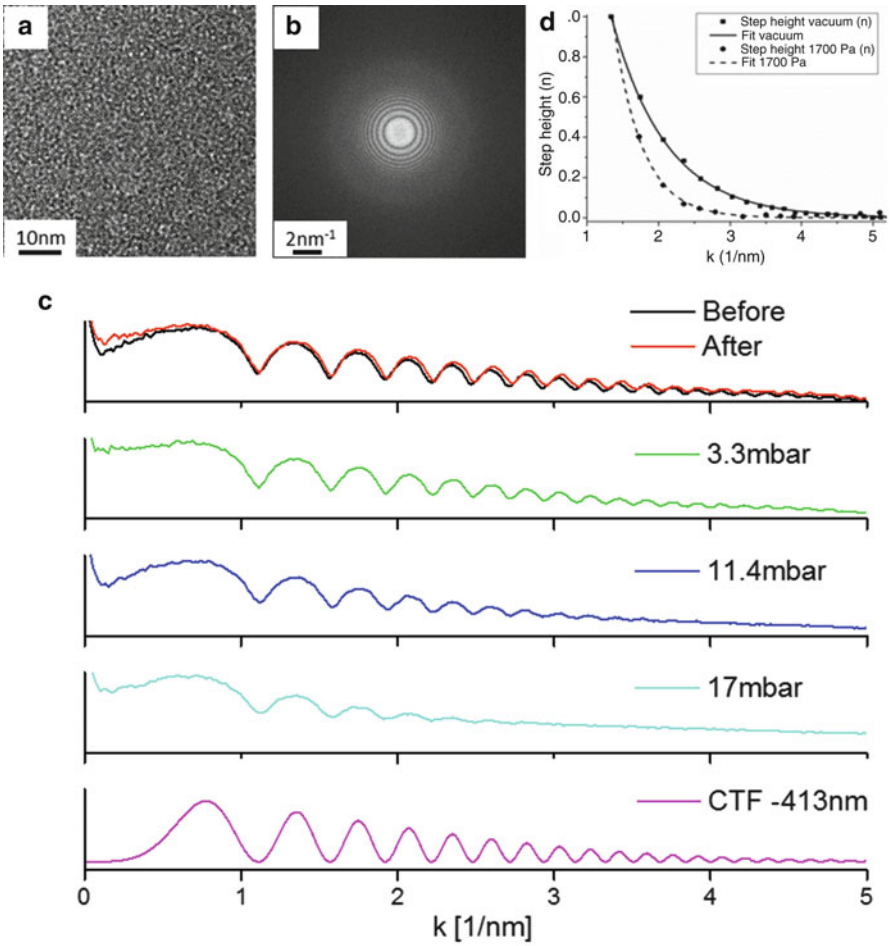

Fig. 3.4 Contrast transfer in presence of gas. (**a**) Amorphous carbon imaged out of focus. (**b**) Fourier transform of (**a**) showing the Thon rings. (**c**) From the FFT in (**b**), the radial intensity has been extracted. Values at intermediate pressures and a simulation made using CTFExplorer (Sidorov 2003) are also included in the plot. (**d**) The step height defined as peak to valley value of the radial intensity of the FFTs is plotted for vacuum and 1700 Pa Ar. Figure modified from Hansen et al. (2012)

resolution, we acquired images of a pristine amorphous carbon film at increasing gas pressure of argon as shown in Fig. 3.4. Prior to each acquisition the defocus value was adjusted to 410 nm as estimated by the aberration-corrector software from the Thon rings. The small change in calculated defocus value after each change of pressure is accredited to thermal drift as the gas temperature might be slightly different compared to the sample temperature.

The radial intensity profiles of the power spectra shows the minima and maxima well aligned as a result of adjusting the defocus value. The apparent damping of the

information from higher spatial frequencies in the image changes clearly with gas pressure. Due to the large defocus value used for the acquisition, the spatial resolution is far from optimum even in the case of imaging in vacuum. Quantifying the contrast transfer by measuring the step height of the oscillations in the FFT being the top-to-valley value shows that damping of the CTF decreases the information transferred at higher spatial frequencies. In the case of imaging in vacuum, 10 % transfer is observed up to 3.2 nm^{-1}, whereas having 1700 Pa argon between the pole pieces results in the maximum spatial frequency being transferred with at least 10 % being around 2 nm^{-1}. Similar observations (not shown here) at 80 kV show a much faster decrease of the contrast transfer. In the presence of lighter gas molecules, this dampening is significantly less pronounced.

A more severe effect of the presence of gas around the sample is damage on the sample and support film primarily in the form of etching, which can be minimized by keeping the beam current density low. For this reason, the current density was deliberately kept low for the present observations, on the order of 1 A/cm^2. The effect on the amorphous film was monitored by recording an image in vacuum after the experiment. The FFT of this image indicates that the damage sustained by the film was insignificant as observed from Fig. 3.4.

The loss of lattice fringe resolution as a function of pressure can be described in terms of a damping of the Contrast Transfer Function (CTF). The scattering events taking place in the high-pressure zone is represented by the CTFs. Energy spread by inelastic scattering induces the defocus Δf due to chromatic aberration and the elastic scattering alters the wave direction Δk leading to an increment in the angular spread. Both leads to damping of the CTF as described by Yaguchi et al. (2011; Suzuki et al. 2013). An estimation based on the calculated CTFs indicates that resolution is not influenced much by 1×10^4 Pa air in a 1.0 mm gas path length (including 15 nm Si_3N_4 membranes). However increasing the pressure just by a factor of 10 to 1×10^5 Pa essentially kills all phase contrast.

In order to get deeper into the understanding of the gas–electron scattering and its effect on the lattice fringe resolution and intensity, Suzuki et al. divided the gas–electron scattering into two regimes (Suzuki et al. 2013). The gas–electron scattering occurring above the specimen does not influence the coherence of each electron and thereby only the angular deflection and the energy loss deteriorate the construction of the image at the image plane. The gas–electron scattering occurring below the sample results in destruction of the coherence and will thereby not contribute to the information transfer from sample to image.

The loss of resolution in terms of decreasing phase contrast at higher spatial frequencies does not only depend on the gas composition and pressure in the ETEM. The total current in the electron beam is found to influence the spatial resolution keeping the current density (electrons per sample area) constant (Jinschek and Helveg 2012; Bright et al. 2013).

To illustrate the effect of the current density and the total electron beam current on the transferred information and thereby the resolution of the microscope operated with gas surrounding the specimen, amorphous carbon has been imaged in 270 Pa of O_2. The images are acquired at a relative high defocus value in order to

identify a number of Thon rings in the FFTs. In Fig. 3.5, the FFTs achieved from images in the presence of gas at different current density and total beam current are shown. The absolute values of the total beam current and the current density are measured without the presence of gas under given optical conditions, which then is used for imaging in gas as well.

Varying the current density keeping the total current and acquisition time constant results in an increased damping of information at higher spatial frequencies (and thereby the resolution) at lower current densities as shown in Fig. 3.5a. This phenomenon is related to the loss of intensity as the signal-to-noise ratio (SNR) is becoming smaller at lower dose. Repeating this experiment without the

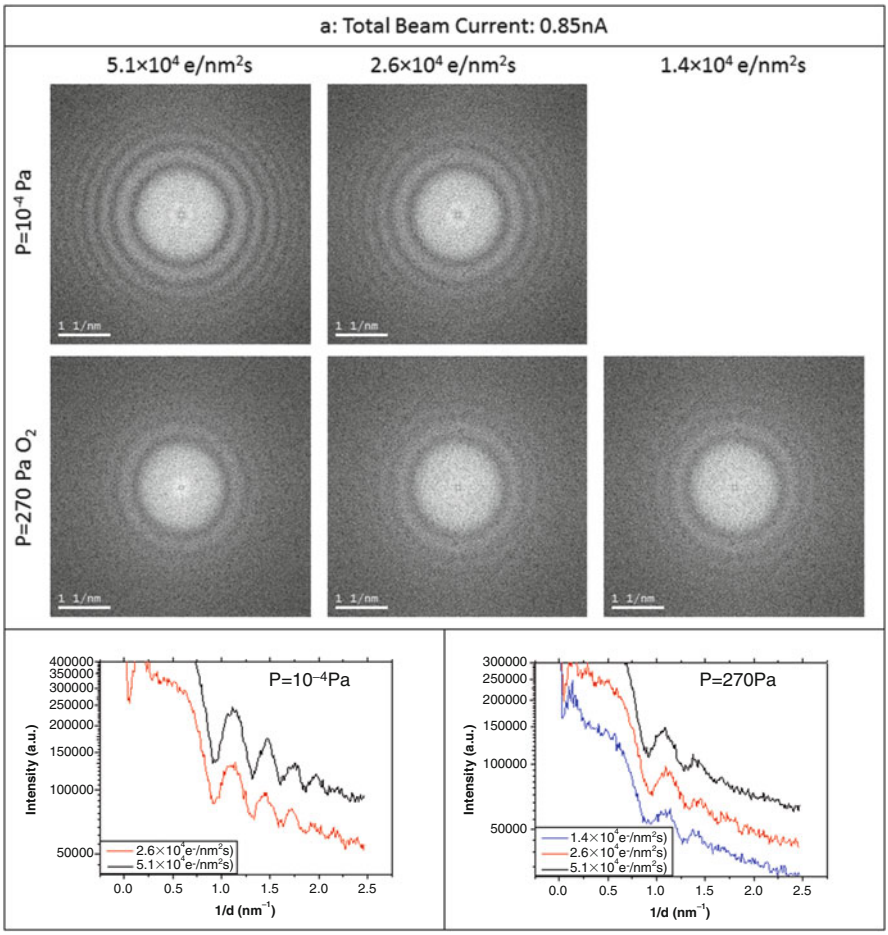

Fig. 3.5 Fast Fourier transforms of images of amorphous carbon as a function of (**a**) current density and (**b**) total beam current. The damping of the information transferred to the image is highly dependent on the total electron beam current in the presence of gas. The resolution of the images acquired in conventional vacuum mode do not show the same dependency

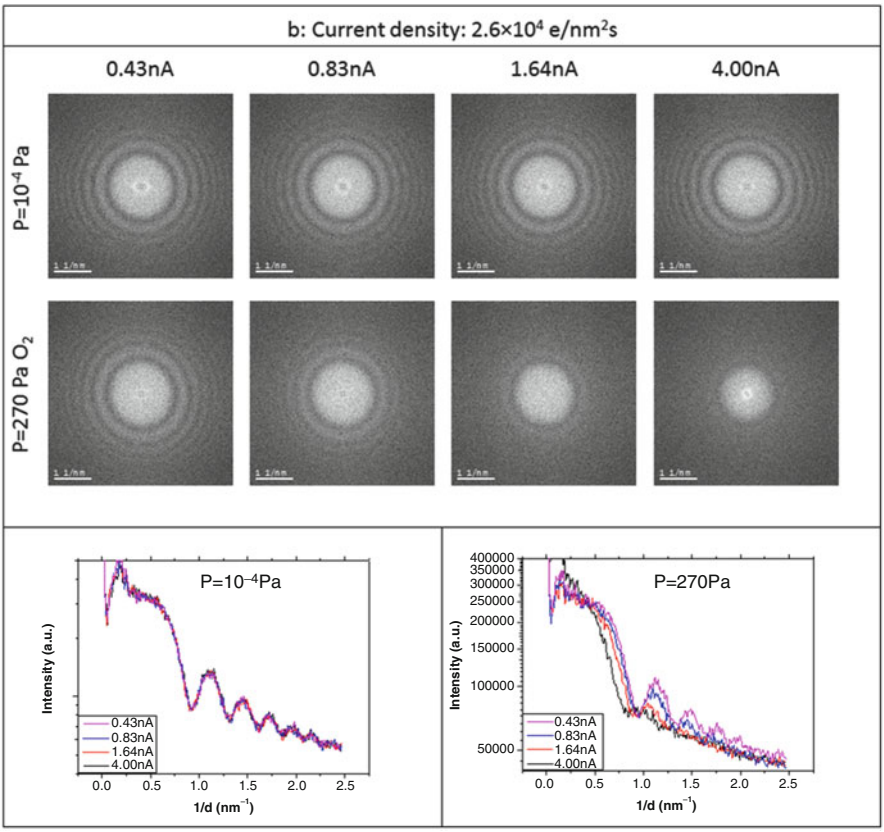

Fig. 3.5 (continued)

presence of surrounding gas molecules gives a similar effect information transfer at high spatial frequencies; however, the SNR is in general higher as the absolute number of electrons contributing to the image is significantly higher without the gas present as seen from Fig. 3.3. Although the SNR plays a role in the loss of resolution, it cannot account for the full effect. Images acquired with similar acquisition time resulting in similar total count on the CCD and similar SNR shows poorer spatial resolution in the presence of gas compared to vacuum in terms of information transfer at high spatial frequencies.

Keeping the current density constant but changing the total current of the electron beam (by changing condenser aperture) results in a significant loss of resolution at higher total beam current in the presence of gas as shown in Fig. 3.5b. The SNR is not affected significantly by the varying total beam current and is observed for a current density range spanning several orders of magnitude (Fig. 3.5; Bright et al. 2013). The resolution of the acquired images in conventional vacuum mode appears to be independent on the total beam current. The current density of the electron beam is measured on the viewing screen and is calibrated to the sample

plane. The electron trajectories of unscattered electrons give rise to a varying beam diameter throughout the pole piece gap. This implies that the current density in the back focal plane is dependent on the total current, even if the current density in the sample plane is kept constant.

3.2.4 Contrast of Bright field images

The resolution and contrast has been discussed above in terms of phase contrast for high-resolution imaging. However, lot of interesting studies have been done over the past decades by means of lower magnification ETEM (Ross et al. 2005; Zhou et al. 2006, 2012; Kodambaka et al. 2007; Li et al. 2009; Sharma 2009; Jeangros et al. 2010; Nasibulin et al. 2010; Costa et al. 2010; Cabié et al. 2010; Janbroers et al. 2011; DeLaRiva et al. 2013; Hansen et al. 2013; Vendelbo et al. 2014). The loss of intensity will of course influence the image quality, but how is electron–gas scattering and interaction affecting the contrast in low-magnification images?

In order to elucidate the relation between image intensity loss caused by electron–gas scattering and the possible related loss of contrast, an edge of a lacey-carbon amorphous film has been imaged at room temperature for varying argon pressures (Fig. 3.6). The edge of the lacey carbon film shows a contrast reflecting the thickness variation of the film corresponding to three distinct thicknesses (thinnest in the upper right corner). The lower left corner of the image corresponds to vacuum (no sample). The intensity profile of the image measured perpendicular to the edge shows four distinct intensities corresponding to the four distinct thicknesses (named 1–4). The overall intensity of the area of interest strongly depends on the total pressure of argon. The intensity decreases by more than 60 % for pressures above 1000 Pa in good agreement with the data presented in Fig. 3.3—the acceleration voltage of the present measurements is 300 kV. Normalizing the intensity of the images to the value measured in the region without any solid sample present (Region 1) shows that the contrast is much less affected. Besides a small spatial shift in the intensity measured between Region 2 and 3 caused by sample drift and possible etching, the contrast remains constant over the pressure range used. The extra scattering of electrons in the presence of gas does not affect the mass-thickness contrast; however, the signal to noise is decreased with increasing gas pressure.

The measurements presented in Fig. 3.6 were all acquired with an objective aperture corresponding to an acceptance angle of 2.7 mrad. The contrast in low-magnification images is strongly related to the size of the objective aperture as it filters the specimen-scattered electrons. Figure 3.7 shows the plot of the intensity measured around a lacey carbon edge. Without any gas present in the microscope column, the image intensity measured at the solid sample decreases with decreasing objective aperture size (Region 2 and 3). As no scattering occurs in Region 1 of the image (without gas) the intensity is constant with varying objective aperture size.

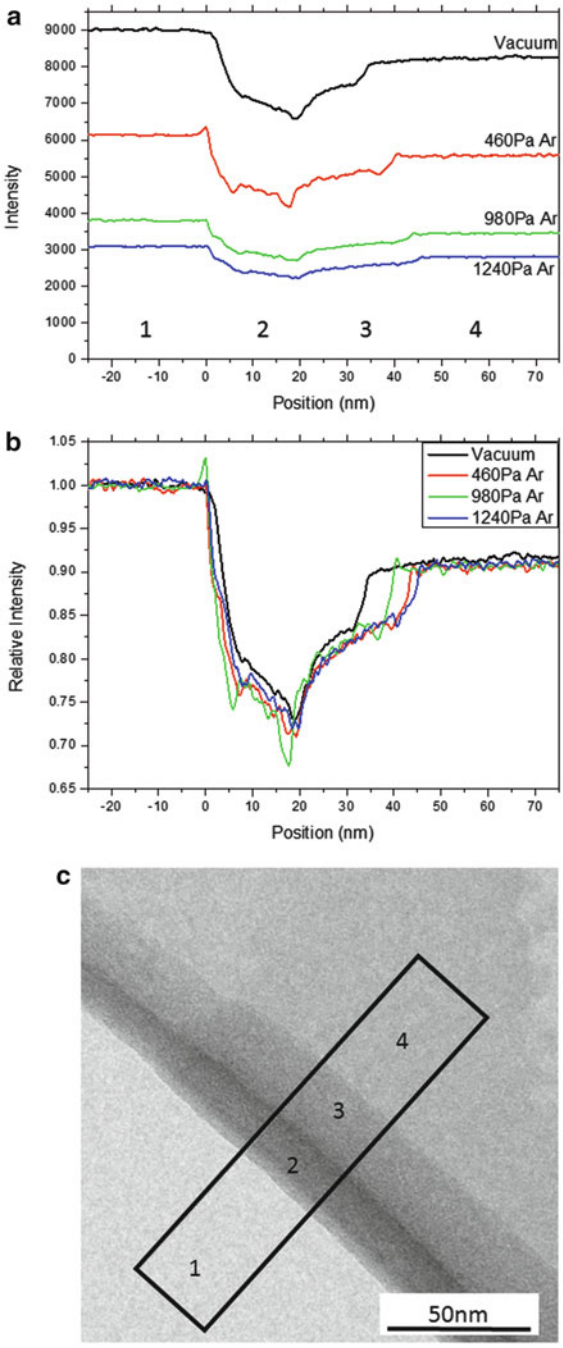

Fig. 3.6 Contrast of amorphous carbon film imaged in presence of Argon. (**a**) Absolute intensity measured on images. (**b**) Normalized intensity revealing an insignificant change in the contrast. The slight shift in intensity around 40 nm is due to sample drift and damage. The numbers 1–4 in the plots refer to the areas indicated in (**c**)

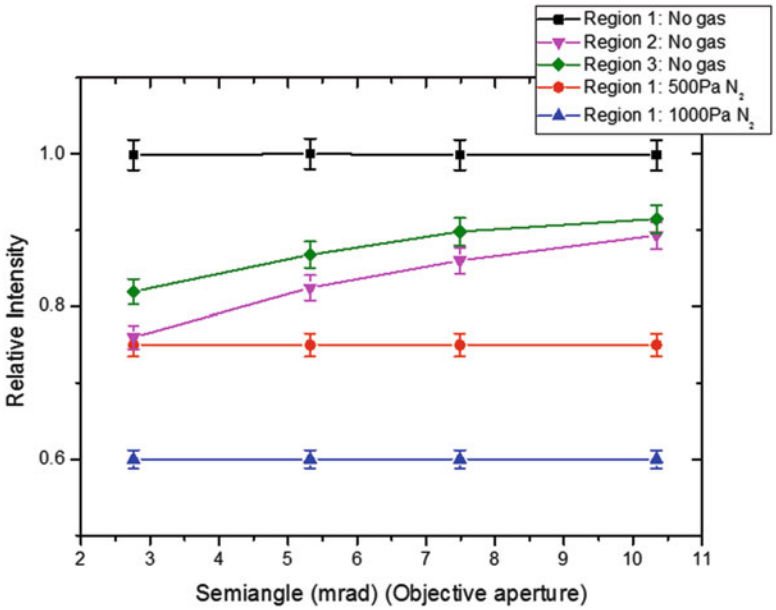

Fig. 3.7 The relative intensity of the carbon edge images in vacuum and nitrogen presented as function of the maximum allowed scattering angle for the electrons forming the image as defined by the objective aperture. The region numbers in the legend refer to the areas defined in Fig. 3.7

Changing the objective aperture in the presence of gas does not have the same effect on the contrast of the image. The intensity is constant with varying objective aperture size in depicted area without any solid sample (as seen in Fig. 3.7). As the scattering of the electrons on the gas molecules takes place over the full gas path between the pole pieces and not only in the plane of the solid sample (see Fig. 3.2), the objective aperture is no longer placed in the back focal plane of the scattering event (object plane).

Furthermore, comparing the intensity of the image in the presence of gas to the intensity measured of the solid carbon sample gives another indication of the ill-defined scattering geometry. Assuming that a gas path of 7 mm of 500 Pa and 1000 Pa N_2 has a projected atom density similar to 5 nm and 10 nm of solid, respectively, justifies the comparison of the measured intensity of the imaged solid without gas present and the measured intensity of imaged gas without solid present. The measured intensity of the gas-only scattered electrons is significantly lower than the measured intensity of the solid-only scattered electrons as illustrated in Fig. 3.7.

This indicates that the limiting aperture for electrons scattered on the gas molecules present in a distance from the sample plane is relatively small (in angular terms) compared to the “normal” objective aperture.

3.3 On the Propagation of Electrons in an ETEM

The observed independence, within experimental uncertainties, of the total current reaching the detector on the objective aperture radius (Fig. 3.7), coupled with the pressure-dependent net loss of electrons (Fig. 3.3), has two important consequences: (1) the angular distribution of the electron beam appears to be very narrow in spite of electron–gas scattering and (2) what "absorbs" electrons cannot be the objective aperture. To explain these findings, we need to move beyond the simple picture of a neutral gas modeled essentially as a low-density amorphous slab with thickness equal to the extension of the gas chamber. In fact, the characteristic elastic scattering angle θ_0 from typical low-Z atomic or molecular gasses (e.g., O_2, N_2, and Ar) is typically of the order of 15 mrad: following Egerton's (1996) introduction to elastic scattering based on the Lenz (1954) model, $\theta_0 = (\lambda Z^{1/3})/(2\pi a_0)$, or $\theta_0 = 6\,Z^{1/3}$ if measured in mrad and with 300 kV electrons, resulting in, for example, about 15 mrad for O_2. Since the fraction of electrons elastically scattered at angles beyond θ_0 is, by definition, 50 %, an Objective Aperture (OA) will necessarily start "absorbing" electrons when its radius approaches θ_0. On the contrary, the data (see Fig. 3.7) indicates unequivocally that no electrons are intercepted in the OA plane outside a very narrow window of just 2 mrad (the smallest aperture used was 10 μm in diameter, located approximately 2.5 mm below the sample plane, giving about 5 μm/2.5 mm = 2 mrad radius). Possible geometrical adjustments, such as considering scattering events happening higher up in the gas chamber, resulting in an effective z-dependent aperture angular radius, are not a sufficient reconciliation. In fact, if the objective aperture physical radius is selected to allow any $<$15 mrad scattered electrons from the sample plane, any electron that is 15 mrad scattered above or below the sample plane will not intercept the aperture.

This can be seen from the diagram in Fig. 3.8, where we calculated the effective aperture radius for axial electrons 15 mrad scattered from an arbitrary location within the 7.5 mm wide gas chamber (indicated by the blue vertical dashed lines). In the diagram, distances are measured from the objective lens mid-gap ($z = 0$ mm), the horizontal dashed line gives the 15 mrad reference, the sample plane (indicated by the purple line) is positioned to receive planar illumination from the nearest cross-over (located above the entrance aperture of the gas chamber at $z = -4.7$ mm for the chosen parameter set) and to form its Fraunhofer diffraction pattern at the OA plane (red line), located at $z = 2.5$ mm. As evident from the diagram, no gas-scattered electron will be absorbed by the OA just because it was scattered above or below the sample: gas-scattered electrons above the sample will be kept within the OA mainly by the focusing effect of the Objective Lens (OL), while those scattered below the sample will effectively see a larger and larger aperture as the location of the scattering event approaches the OA plane. Those electrons that are scattered below the OA plane (where there is still gas) will obviously see no aperture at all. The focusing effect of the pre-field is particularly important in determining the effective aperture size, as just by considering straight trajectories and the geometrical angles involved, one would expect a portion of the electrons

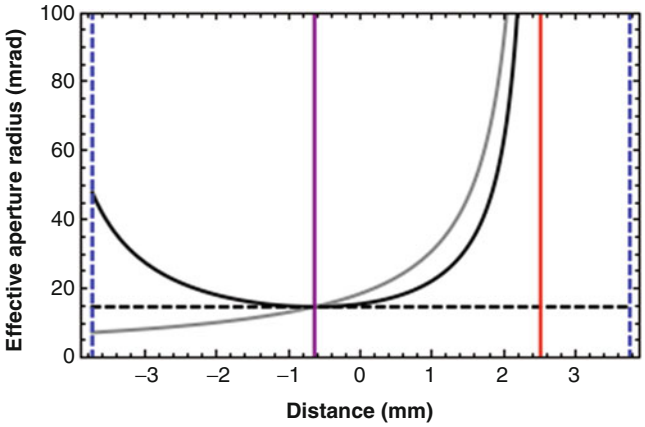

Fig. 3.8 Effective angular size (*black line*) of a nominal 15 mrad objective aperture (*black dashed line*) when referred to a scattering event occurring within the gas chamber at a coordinate z along the optic axis. The curve differs from a simple geometrical estimate based on straight trajectories (*gray line*) due to the focusing effect of the objective lens' field. Additional *colored lines* indicate the position of sample plane (*purple*), objective aperture plane (*red*), and pressure-limiting apertures (*dashed blue*)

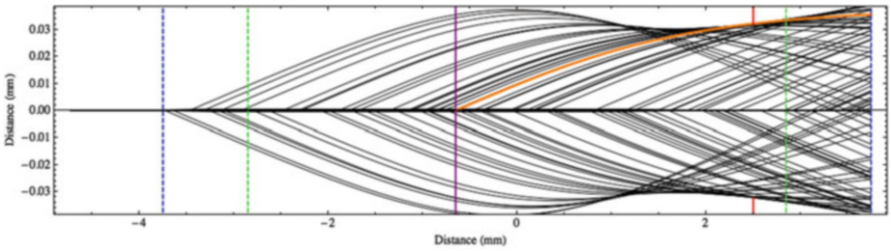

Fig. 3.9 Set of trajectories representing electrons scattered at 15 mrad from a random location along the optic axis illustrating how, regardless of where scattering occurs, no electron is intercepted by the objective aperture (*red line*). The *orange line* highlights a 15 mrad scattering event originating at the sample plane (*purple line*), reaching precisely the edge of the objective aperture. *Other colored lines* indicate the positions of the pressure-limiting apertures (*blue*), and objective lens pole pieces (*green*)

scattered above the sample to be intercepted by the aperture, as illustrated by the gray line.

To further illustrate the concept and role of an effective position-dependent aperture size, we have calculated a set of 10,000 trajectories (100 of which are plotted in Fig. 3.9) for electrons that are scattered at 15 mrad from a random location along the optic axis within the gas chamber. In Fig. 3.9, we have added a 15 mrad "Bragg beam" (thick orange line) originating from the sample and used to choose the appropriate OA radius (about 30 μm in this case). We have also added two dashed green lines indicating the positions of the pole pieces bounding the OL gap. A standard Glaser

model was used for the OL field ($B_{max} = 2.2$ T, $a =$ OL gap/2 $= 2.85$ mm) to facilitate the computation.

Visual inspection of Fig. 3.9 reveals an important piece of information: while pre-sample scattering does not remove electrons from the beam, it does influence dramatically the illumination characteristics. In absence of gas scattering, and with the chosen electron-optical setup (position of the cross-over, position of the sample, OL axial field model, etc.) the sample would be illuminated by a 1-μm patch of planar illumination, while electrons scattered at 15 mrad higher up in the gas chamber, may end up as far as 30 μm off-axis at the sample plane. This simple observations hints already at what might be responsible for the observed net decrease of electrons reaching the CCD: a field-limiting aperture positioned further down the column, for example, the selected area aperture (SAA), or one of the entrance diaphragm of the image-corrector. This is better visualized by zooming the trajectory plot out to the first image plane, in this case located about 6 cm down the column.

Figure 3.10 reveals that the reference "Bragg beam" originating at the sample plane makes its way through the OA, and is kept paraxial down to the image plane where it recombines with all other beams from the sample to form the image. The rightmost purple line indicates the position of the image plane, and it has an aperture that corresponds to the 1-μm illumination patch on the sample plane once rescaled for the OL magnification factor. Almost all trajectories, corresponding to electrons scattered at almost any position other than the sample plane, are intercepted by the purple field-limiting aperture. Some electrons are also intercepted by the lower 400-μm pressure-limiting aperture positioned 17 mm below the first one (both indicated by the blue lines in the illustration).

The considerations exposed so far provide us with a qualitative explanation as to why the OA plays no role in "absorbing" gas-scattered electrons while at the same time the net count reaching the detector may be very small. However, the data underpinning this analysis tell us that the OA plays no role even for angular apertures much smaller than the expected neutral-gas characteristic elastic

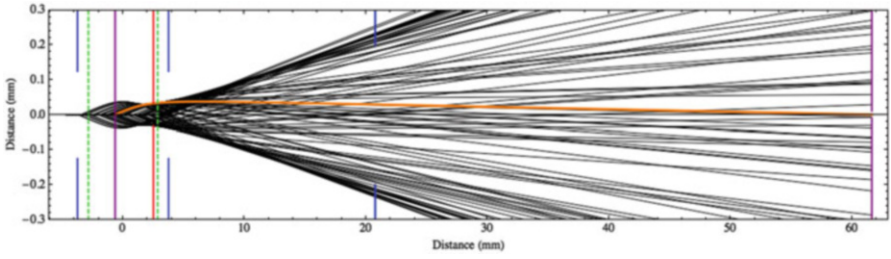

Fig 3.10 Same set of trajectories as in Fig. 3.9, plotted over a larger scale and illustrating the importance of further apertures positioned down the column. The third *blue line* at $z = 70$ mm indicates a 400 μm aperture that is part of the ETEM system, while the second *purple line*, positioned at the image plane, indicates a field-limiting aperture (selected area-type) conjugate with the 1 μm illumination patch on the sample

scattering angle, and this is clearly at odds with the diagrams presented above: if we imagine to reduce the OA radius from 30 μm down to 5 μm (the smallest OA used), while keeping the gas-scattered electrons at 15 mrad, we would definitely start "absorbing" electrons directly in the OA plane.

Since the analysis of the effective position-dependent aperture revealed that the nominal aperture angular radius (referred to scattering from the sample plane) is a lower limit, in the sense that it is effectively bigger for electrons that are gas-scattered anywhere else within the gas chamber, we can only conclude that the characteristic angle for gas scattering is much smaller than what we estimated on the basis of the Lenz model. Since the atomic weight of the gas is fixed, and so are temperature, pressure, and beam energy, the only parameter that might result in a substantial decrease of the characteristic angle is ionization of the gas. We may imagine, in fact, that as soon as the beam is turned on and electrons start crossing the gas chamber, a fraction of them will undergo inelastic scattering while ionizing the gas. In fact, ionization losses are clearly observed in the EELS signal (see Chap. 4), indicating that the primaries trigger and sustain the generation of free electrons and ions in the chamber; their recombination will then kick-in, until a dynamic steady-state equilibrium is reached in the form of a plasma. The charge-carrier density of the plasma will depend on generation and recombination rates, and it is important to estimate the beam-induced plasma characteristics, in particular its Debye length, because the typical elastic scattering angle will depend on it.

In a single-scattering approximation, by combining the stopping power S (in units of energy/length) of the gas as given by the NIST ESTAR database (Berger et al. 2005) the mean observed energy loss E_i associated with ionization of the gas molecules, and a primary beam current density J_p, we can write the volume generation rate G (in units of number density per unit time, or $1/(\mathrm{m}^3\mathrm{s})$) of electrons as

$$eG = J_\mathrm{p} S / E_\mathrm{i}$$

For example, considering $P = 1$ mbar He at room temperature, having a number density of $n_\mathrm{He} = P/k_\mathrm{B}T = 2.4 \times 10^{22}/\mathrm{m}^3$ (equivalent to a mass density of $4n_\mathrm{He}u = 1.6 \times 10^{-7}\ \mathrm{g/cm}^3$) ESTAR estimates a stopping power for 300 keV electrons of about 36 eV/m, corresponding to a mean loss of 0.27 eV (or 11 ionization events per 1000 primaries) over the 7.5 mm gas chamber. The generation rate according to (3.1) considering a primary current density of 16 $\mathrm{kA/m}^2$ and the He ionization energy $E_\mathrm{i} = 25$ eV is then $G = 1.5 \times 10^{23}\ 1/\mathrm{m}^3\mathrm{s}$, which is a very small number: for comparison, the typical electron-hole pair generation rate in a solar cell under solar illumination can be 5–7 orders of magnitude higher, and EBIC effects with solid targets might originate from even larger generation rates. Of course, such a large difference arises from the low gas density with respect to that typical of solids.

The generated electrons and ions, in the example above He^+, will start recombining, and a steady state is reached when the generation and recombination rates are equal. Considering a recombination term with the form Knp, and noting that in this simple picture that disregards the variety of ionic species and charge

states that are interacting and evolving in higher-Z molecular gasses, the electron and He^+ densities are equal, i.e., $n = p$, the plasma charge density at steady state is simply $n_p = (G/K)^{1/2}$. A representative value for the recombination constant K (Fugol et al. 1971) is about 1×10^{-15} m^3/s at room T, independent on P, giving a plasma density of just $n_p = 1.2 \times 10^{19}\,m^{-3}$, corresponding to an average gas ionization degree $n_p/n_{He} = 250$ ppm. The characteristic time for achieving the steady state can be estimated as $\tau = (GK)^{-1/2}$, or 75 μs.

Increasing the gas pressure fourfold leads to a 4× larger gas density, 4× higher generation rate, 2× larger plasma density, 2× faster steady state achievement, and 2× *smaller* degree of ionization.

Having neglected generation of higher ionic charge states, as well as core-losses and secondary ionization, the estimated plasma density is most likely a lower bound. We have also considered one particular beam current density in this example, representative of the value it has near the sample plane in our experiments. The simple equation $G = Kn^2$ we have employed to predict the steady state plasma density is the residual term of the drift-diffusion transport equation when both drift and diffusion are absent, i.e., when the charge density in the plasma is uniform, so that no electric fields and no concentration gradients are present. However, as the beam converges towards the focal point, the beam current increases by orders of magnitude, and so does the generation rate, leading to a higher plasma density in the OA plane. Even more rapid is the decay of the primary current density at the rim of the illumination patch, where the generation rate drops to zero over a sub-micron length scale. As a consequence, we cannot expect a uniform charge concentration throughout the gas chamber, which triggers diffusion followed by the formation of space-charge regions with non-negligible electric fields that, in turns, may modify the whole electron-optical configuration in the OL field region. In particular, measurable variations of the focal length are conceivable due to the plasma field acting as a weak electrostatic lens on top of the much stronger OL. Achieving a satisfactory description of the beam-induced plasma in the gas chamber requires necessarily the full, self-consistent solution of the drift-diffusion equation in a circularly symmetric three-dimensional volume with the spatially varying magnetic field of the OL included as an additional term as it affects the plasma dynamics. As this treatment is beyond the scope of this chapter, we extend the basic picture developed so far only by considering, when needed, a z-dependence of the plasma density according to

$$n_p(z) = [J_p(z)S/(eKE_i)]^{1/2}$$

while abandoning any quantitative intention.

Once equilibrium is reached, free electrons wandering in the gas chambers start playing a fundamental role: screening of the ionic Coulomb potential. As it happens in any physical system with co-existing charge carriers of opposite sign in a dynamic equilibrium, for example, in semiconductors, electrolytes, or in the ionosphere of our planet, an added external charge polarizes the environment resulting

in an electric field that decays with distance faster than in vacuum. In particular, the Coulomb potential of an isolated charge in vacuum turns into a Yukawa potential, also called "screened Coulomb potential"

$$V(r) = e/(4\pi\varepsilon_0 r)\exp(-r/\lambda_D)$$

decaying exponentially over a length scale λ_D named "Debye length," which is defined for a Maxwellian free electron gas with fixed neutralizing background ("jellium" model) as

$$\lambda_D = \left(\varepsilon_0 k_B T/n_p e^2\right)^{1/2}$$

For the 1.2×10^{19} 1/m^3 He plasma density calculated earlier when the pressure is 1 mbar, the resulting Debye length at room T is approximately 350 nm. Since the plasma density depends on the square root of pressure via the stopping power, and the Debye length depends on the inverse square root of the plasma density, ultimately we have a relatively weak dependence of λ_D on pressure, i.e., $\lambda_D \sim P^{-1/4}$. At 10 mbar pressure, for example, the Debye length is about 200 nm. As we illustrate in the following, plasma screening occurring at a Debye length scale is the key concept needed to address the puzzling experimental results, as it affects dramatically the mean elastic scattering angle we expect from a partially ionized gas.

The elastic cross sections for electron scattering by ions are very different from those for neutral atoms. As shown by Peng et al. (2004), ionic scattering factors for an atomic number Z are decomposed into two terms: the first arising from the fully screened atom potential $f_0(q)$ for a virtual neutral atom with atomic number $Z - Z_i$, (Z_i is the ionic charge) the second originating from the long-range Coulomb potential of a bare point charge with magnitude Z_i, and resulting in a pure Rutherford term:

$$f_{\text{ion}}(q) = f_0(q) + 2\gamma Z_i/\left(a_0 q^2\right)$$

where a_0 is the Bohr radius and $q = 4\pi/\lambda \sin(\theta/2)$ is the magnitude of the momentum transfer for a scattering angle θ. Note that we have adopted the notation of Egerton (1996), while scattering factors in Peng et al. (2004) are tabulated as a function of $s = \sin(\theta/4)/\lambda$ rather than as a function of q. At small angles, s and q are simply related by $q = 8\pi s$.

As visible in Fig. 3.11, where we consider Au only for illustration purposes since its scattering factors are readily available, neutral atom and ionic scattering factors differ in particular at small angles due to the long-range potential of the unscreened ionic charge capturing electrons at large impact parameters. The small-angle divergence of the Rutherford cross section for an isolated charge poses a normalization problem. Having a finite total cross section is a necessary prerequisite for proper accounting of the incoming vs. scattered electrons: if the cross section goes

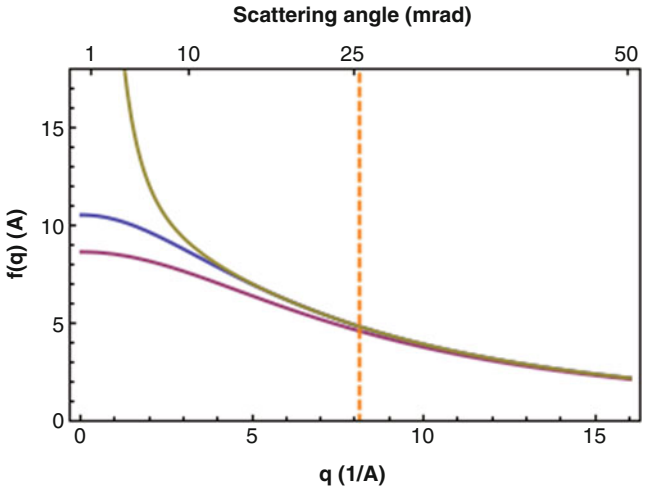

Fig. 3.11 Scattering factor for neutral Au (*blue curve*) and Au+ (*yellow curve*). The purple curve represents $f_0(q)$, originating from the screened portion of the atom potential. The dashed orange line indicates the characteristic elastic scattering angle for neutral Au, $\theta_0 = 6 \times 79^{1/3} = 25$ mrad, corresponding to $q = 8.1$ A^{-1} for 300 keV electrons

to infinity, every electron, no matter how far from the ion, is captured and undergoes elastic scattering, although essentially all of them are scattered at very small angles.

In plasmas, however, as discussed above, screening provides a cutoff that keeps the total cross section finite. To estimate the characteristic plasma-scattering angle, we proceed heuristically. For neutral atoms, the large-angle (low impact parameter) cross section is Rutherford, while for small angle it is dictated by Thomas-Fermi screening of the nucleus potential over a characteristic length $r_0 = a_0 Z^{-1/3}$ (as already used above when estimating θ_0). For ions in a plasma, large-angle scattering remains Rutherford, but small-angle scattering now becomes, and this is our ansatz, Debye-screening limited, with characteristic length set by the plasma density-dependent Debye length.

If we then revisit the derivation of the scattering factor in presence of a different type of Yukawa potential, with screening parameter now equal to the Debye length in the plasma, we obtain an approximation for the elastic cross section from ions, which remains finite at $q \to 0$ and allows to calculate the total cross section thereby giving us the opportunity to estimate the effect of ionization on the beam.

Modifying then the Rutherford term in the ionic scattering factor by replacing q^2 with $q^2 + \lambda_D^{-2}$, and estimating the screened term $f_0(q)$ as if it originated from a neutral atom with atomic number $Z - Z_i$, we arrive at

$$f_{\text{ion}}(q) = 2\gamma/a_0 \left[(Z - Z_i)/\left(q^2 + r_0^{-2}\right) + Z_i/\left(q^2 + \lambda_D^{-2}\right) \right]$$

Note that $f_{\text{ion}}(q) \to f(q)$ when either $Z_i = 0$ or $\lambda_D \to r_0$.

Since the differential cross section is the square modulus of the scattering amplitude, by integrating $|f_{\text{ion}}(q)|^2$ over the unit sphere we obtain the total elastic cross section of a Debye-limited ion, of which we keep only the (overwhelmingly) dominant term proportional to λ_D:

$$\sigma_{\text{e,ion}} = 4\pi\gamma^2 Z_i^2 \lambda_D^2 / \left(a_0^2 k_0^2\right)$$

to be compared with the neutral atom total elastic cross section calculated within the Lenz model

$$\sigma_e = 4\pi\gamma^2 Z^{4/3} / k_0^2$$

Since, the ratio $\sigma_{\text{e,ion}}/\sigma_e$ is proportional to λ_D^2/a_0^2, and the Debye length, typically sub-micron as found earlier, we conclude that the elastic cross section is plasma-enhanced by several orders of magnitude. Imagining the total cross section as a circle, its radius expands from something at the Angstrom scale, to something much larger, comparable or larger than the beam size (depending on where we are along the optic axis). While consistent with the diverging trend of the Rutherford cross section for an unscreened charge, this implies that we cannot remain in the single-scattering approximation, or consider concepts such as "fraction of scattered (or unscattered) electrons," "scattering probability" as meaningful in presence of an ionized gas, even when the degree of ionization is low. In fact, reconsidering the plasma density (250 ppm of the gas number density) obtained at 1 mbar pressure, this corresponds on average to just a few ions per cubic micron, and therefore every primary will be elastically scattered several thousand times over its 7.5 mm long path within the gas chamber. Each time, the angular distribution broadens a little according to a Lorentzian-type probability density function, exactly as from a neutral atom, except that the characteristic angle now is $\theta_p = 1/(k_0\lambda_D)$ instead of $\theta_0 = 1/(k_0 r_0)$. For 300 keV electrons and $\lambda_D = 350$ nm, $\theta_p = 1$ μrad.

We have plotted in Fig. 3.12 ten unscattered (grey curves) and 1-μrad scattered (orange curve) trajectories for electrons traversing the gas chamber (bounded by the blue dashed lines) under the influence of the OL field (OL gap bounded by the green

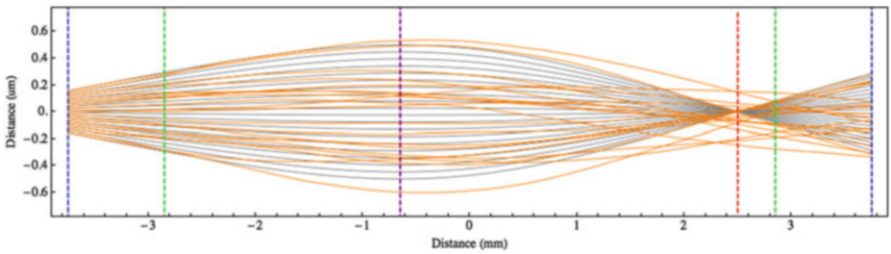

Fig. 3.12 Unscattered (*gray*) and 1-μrad gas-scattered (*orange*) trajectories within the gas chamber. The effects of gas scattering are visible both at the sample plane (*purple line*) and at the OA plane (*red line*), as the spatial and angular distributions of the illumination broaden progressively

dashed lines). As before, the electron-optical configuration was chosen to simulate a 1-μm patch of planar illumination at the sample plane (indicated by the dashed purple curve) forming its Fraunhofer pattern at the OA plane (red dashed line). Scattered and unscattered trajectories coincide at the entrance aperture of the chamber, and they progressively differentiate as scattering from the gas ions accumulates.

To better visualize how the beam evolves in presence of gas, we have sampled the spatial and angular distribution of the beam in the sample, OA and image plane, and created histograms representing the beam spatial and angular profiles in those planes. The histograms are shown in Fig. 3.13, for He pressure of 1 and 20 mbar, corresponding to mean scattering angles of 1 and 2 μrad, respectively. As sketched in Fig. 3.13, in absence of scattering the beam has a top-hat/delta (spatial/angular) profile in the sample plane, a delta/top-hat profile in the OA plane, and a top-hat/top-hat profile in the image plane. Gas scattering broadens progressively all distributions, with the most significant effect occurring in the image plane where about 11 % of the incoming electrons are transferred outside the illumination patch, thereby lowering proportionally the observed intensity per pixel around the central portion of the illuminated area.

3.3.1 *Influence on Material Observations*

As discussed above, scattering of electrons on the gas molecules present near the sample of interest in environmental TEM has a significant impact on the microscope performance. However, the interaction between the gas and fast primary electrons as well as secondary electrons might change the properties of the gaseous environment and thereby lead to artefacts in the sample observations.

However, the combination of the electron beam and gas molecules in the transmission electron microscope can been used for electron beam-induced deposition (van Dorp et al. 2011) and is thereby not always to be considered as an artefact.

In the following, a few examples of the more indirect influence on the microscopy observations originating from the interactions between the gas molecules and the free electrons are discussed.

3.3.2 *Ionization of Gas Molecules*

Damage or modifications of the observed samples due to the, at times, high current density is a well-documented phenomenon in the electron microscopy society. In general, two types of beam damage are considered in the TEM: Knock-on damage and radiolysis. The former is caused by displacement of atoms in the sample by momentum transfer from fast primary electrons to atoms in the sample. Usually,

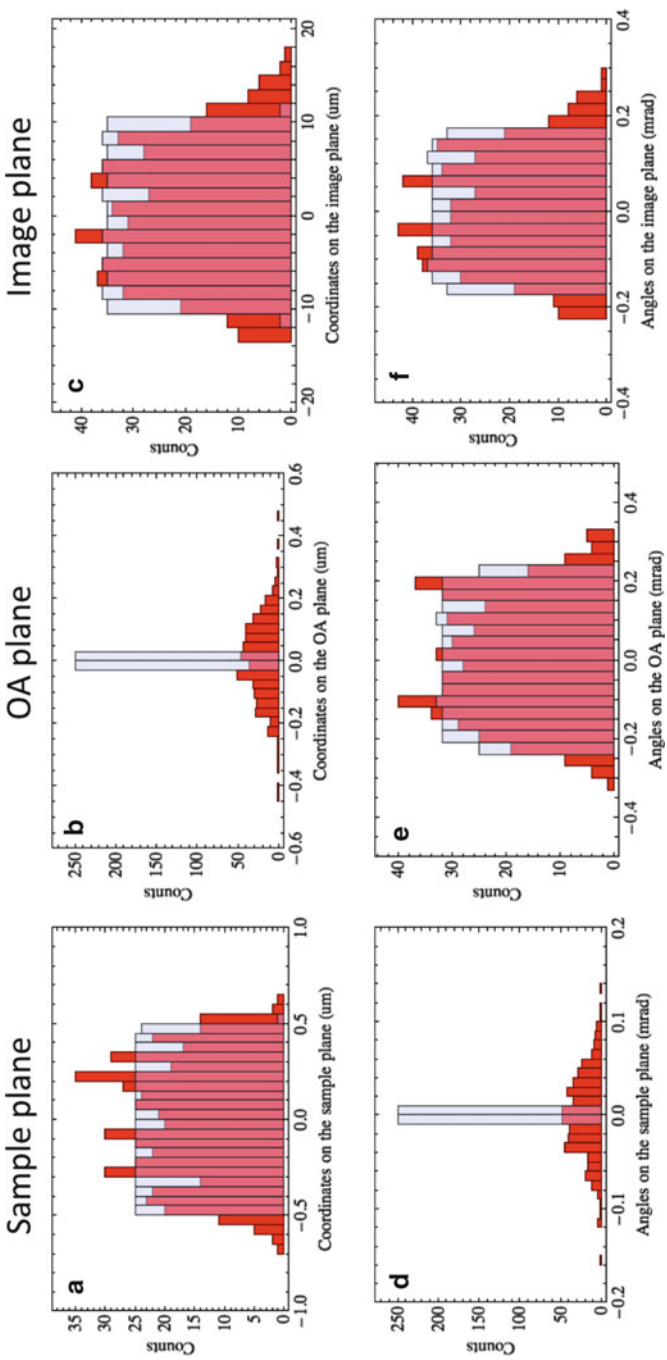

Fig. 3.13 Histograms of the spatial (**a**–**c**) and angular (**d**–**f**) profile of the illumination with (*red bins*) and without (semi-transparent *blue bins*) gas scattering at 1 mbar He pressure. The histograms represent snapshots of the collection of electron trajectories intersecting the three sample (**a**, **d**), OA (**b**, **e**) and image (**c**, **f**) planes

this can be minimized by lowering the energy of the electron beam (Egerton et al. 2010; Smith and Luzzi 2001). Radiolysis is caused by fast electrons modifying the chemical bonds in the sample, leading to changes in the electronic structure and thereby stability of the sample. This type of damage is usually larger for lower electron beam energies due to the larger interaction cross section. Examples of beam-induced chemistry can be found in the electron beam-induced reduction of molybdenum and vanadium oxides as described by Su et al. (Su et al. 2001; Wang et al. 2004). In addition to the beam damage observed in conventional TEM, ionization of gas molecules as a result of the interaction between free electrons and gas leads to increased reactivity. Therefore, it is very important to perform the ETEM experiments as a function of beam current density to explore the effects of ionized gas molecules near the sample.

As an example, the development of MgO smoke particles covered with Au nanoparticles in the presence of water vapor has been studied in situ in the electron microscope. MgO smoke particles produced by ignition of an Mg metal ribbon form close-to-perfect cubes exposing the MgO (100) surfaces. These cubes serve as a perfect substrate for studying nanoparticle-support interactions and especially the interface between. Gold is sputter-coated onto the cubes forming 2–6 nm epitaxially oriented Au nanoparticles.

Figure 3.14 summarizes our findings on the effect of electron dose and water vapor pressure in the vicinity of the sample. All experiments are performed at room temperature. The images are extracted frames from movies after approximately 30 min exposure in each case. At low pressure ($P = 10^{-5}$ Pa) and relative low electron dose rate (0.1 A/cm^2) the surface mobility is observed to be relatively small. In conventional high-vacuum TEM mode (including the use of a cold trap to minimize the water vapor pressure), the column base-pressure is ca. 10^{-5} Pa. Increasing the electron dose or the pressure by leaking in water vapor increases the mobility of MgO species on the surface resulting in the formation of kinks and steps. At increasing water vapor pressure, the species diffusing at the MgO surfaces start to accumulate at the Au/MgO interface. At relatively high electron dose rate (1.0 A/cm^2) and a pressure of 10^{-4} Pa pillars grow from the cubes apparently catalyzed by the Au nanoparticles. Au-catalyzed MgO pillar growth has been reported earlier (Ajayan and Marks 1989; Nasibulin et al. 2010), but in the present study, the effect of the environment has been addressed in greater detail. Even a low partial pressure of water vapor (10^{-5} Pa) has an apparent effect on surface species mobility in the Au/MgO system.

Pure MgO-smoke particles are known to hydroxylate under electron irradiation in the presence of water (Gajdardziska-Josifovska and Sharma 2005) modifying the perfect (100) surfaces of the MgO cubes. MgO species (Mg^+, $(MgO)^+$) are mobile on the surface of the cubes as a result of the energy transferred from both primary and secondary electrons (Kizuka 2001) creating steps and kinks on the MgO (100) surfaces.

The Au/MgO interface acts as a collection point (due to negatively charged metal particles) where the highly mobile MgO species are trapped and recrystallize in pillars. The presence of water species in the surrounding environment influences the charge transfer in the system changing the overall energy landscape. The change in behavior of the system in the presence of water vapor under electron beam

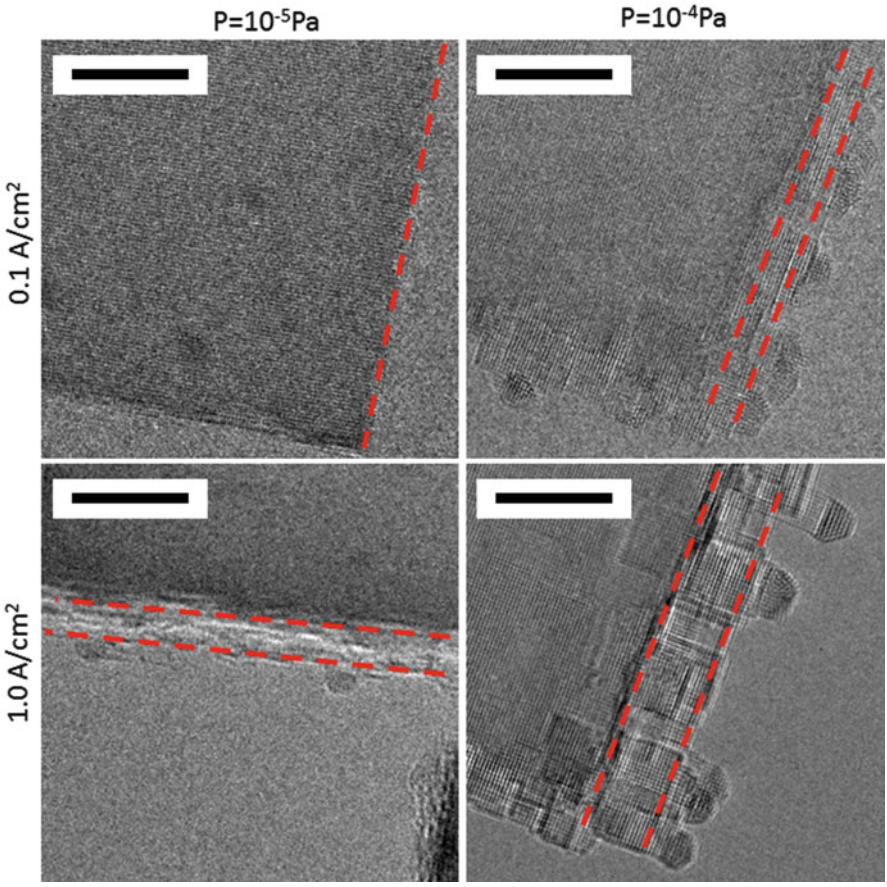

Fig. 3.14 TEM images of Au on MgO smoke cubes. The images are stills extracted from movies acquired at 300 kV in a FEI Titan ETEM. The Au/MgO sample was exposed to different electron dose rates (0.1 and 1.0 A/cm^2) at different pressures (10^{-5} and 10^{-4} Pa) for approximately 30 min in each case. The scale bars are 5 nm. Figure adapted from Duchstein et al. (2014)

irradiation illustrates the necessity for addressing the additional energy and radicals introduced when dealing with gases, even at room temperature. The thresholds of these beam- and gas-induced effects are strongly dependent on the material system and have to be studied systematically in each case.

As illustrated above the presence of gas molecules and especially water, even in low concentration, can change the observation in the electron microscope drastically. Cavalca et al. has been studying the photodegradation of cuprous oxide in the presence of water in situ in the electron microscope by means of a purpose-built TEM sample holder capable of letting light into the microscope in a controlled manner (Cavalca et al. 2012, 2013). The degradation of the cubed cuprous oxide nanoparticles observed by the authors in the presence of water and light to metallic copper is due to electron transfer to water molecules absorbed on the Cu_2O surface.

The electron transfer is facilitated by creation of electro-hole pairs by means of light. The observations had to be performed in a pseudo in situ manner as the electron beam accelerated the process by orders of magnitude. The electron beam did not degrade the Cu_2O nanocubes without the presence of water in the sample vicinity. That implied that imaging of the process had to be performed in the absence of water and a "stop-and-go" protocol was used by alternating between imaging in vacuum and treating the sample in water and the presence of light, but without irradiating the sample with electrons (see also Chap. 8).

It is obvious that extra care has to be taken when performing electron microscopy experiments in the presence of gas. The observations by environmental TEM have to be compared at different beam currents and beam current densities. Ideally, the observations have to be evaluated without the electron beam as well (Hansen et al. 2013). These blank experiments will, together with complementary experiments by other means than electron microscopy, help to justify the observations made in the presence of gas in situ in the microscope (Hansen et al. 2002). An example of the importance of studying the electron beam effect in environmental TEM experiments is reported by Simonsen et al. (2010). The authors studied the electron beam effect on the observation of Pt nanoparticle sintering mediated by Ostwald ripening. The shrinkage rate of Pt nanoparticles supported on Al_2O_3 was measured with an electron beam current density from 0.07 to 1.0 A/cm^2 in the presence of 1000 Pa air at 400 °C. The shrinkage rate showed a clear linear dependency on the beam density in the measured range as viewed in Fig. 3.15. The lack of shrinkage without the electron beam or with electron beam in pure N_2

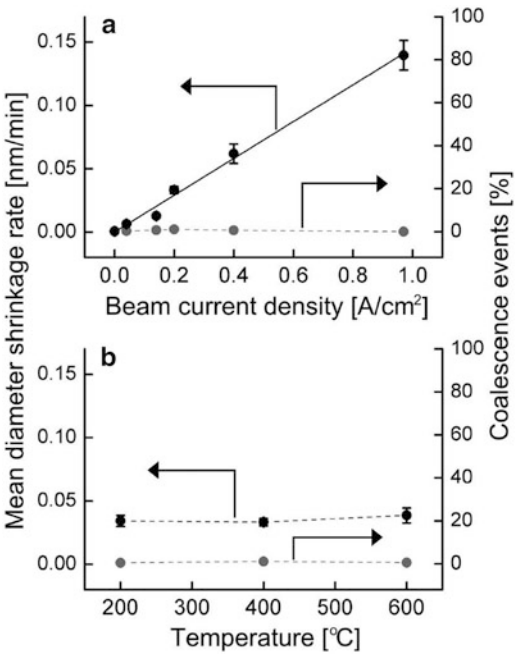

Fig. 3.15 The mean particle diameter shrinkage rate and the number of coalescence events of the Pt/Al_2O_3 catalyst during exposure to 1000 Pa air as a function of beam current density at constant temperature (400 °C). Figure adapted from Simonsen et al. (2010)

concludes that the effect is a combined electron beam and oxidizing gas effect. In order to follow the dynamical time-resolved Ostwald ripening the authors minimized the beam current to 0.07 A/cm^2 and only acquired snapshots during several hours of treatment arguing that the observed electron beam-induced nanoparticle shrinkage could be neglected at the given total electron dose in comparison to the total effect observed.

It is not only the beam current but also the total dose, which plays a role in the electron beam-induced phenomena observed during ETEM experiments. The structure evolution under electron beam irradiation of the Au/TiO_2 system for CO oxidation is studied in detail by Kuwauchi and co-workers (2012). The Au-TiO_2 is found to be strongly influenced by the surrounding gas in combination with the intense electron beam as summarized in Fig. 3.16. In the presence of oxygen or

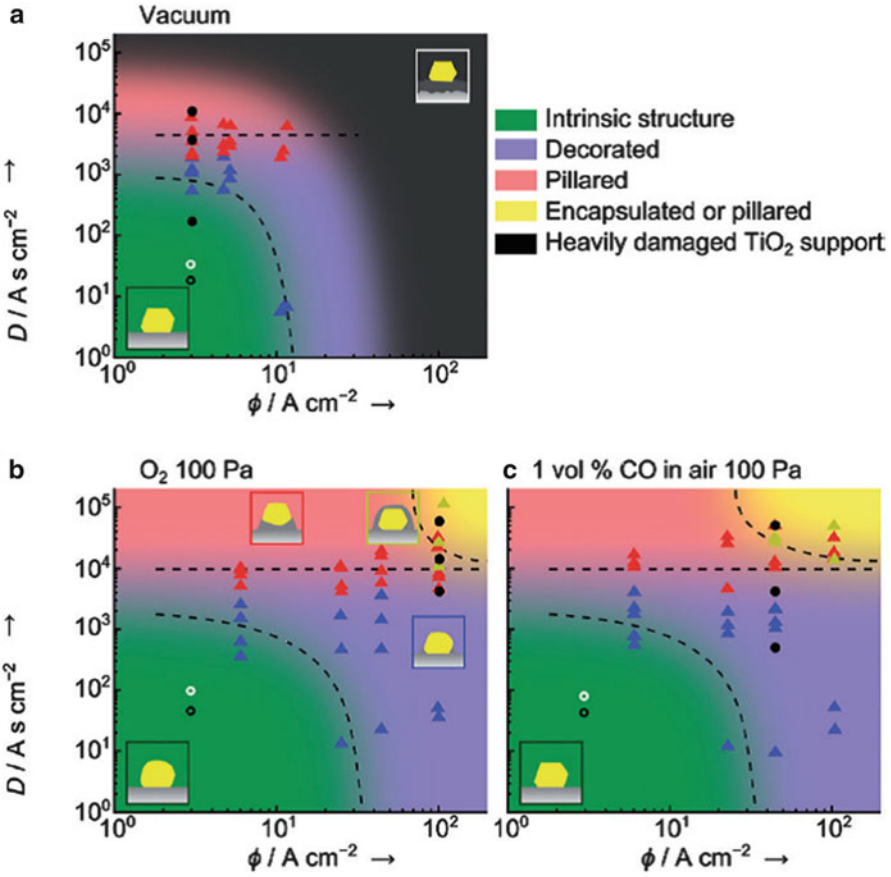

Fig. 3.16 Structural changes of Au/TiO_2 catalyst under different gases varying the electron current density, φ, and the total dose, D, observed in ETEM. (**a**) Vacuum, (**b**) 100 Pa of O_2, (**c**) 100 Pa of CO/air (1:100). All observations at room temperature. The color coding represents the categorized types of structural changes of the Au/TiO_2 system. Figure adapted from Kuwauchi et al. (2012)

carbon monoxide and an intense electron beam, TiO_2 decorates and encapsulates the Au nanoparticles at higher beam current. An interesting observation is that the decoration of Au nanoparticles by TiO_2 is found even without gas present, although at lower beam currents, but the complete encapsulation requires CO or O_2. Increasing the beam current in vacuum results in a heavily damaged TiO_2 support at beam currents above approx. 50 A/cm^2. This is not observed in the presence of CO or O_2 at similar beam currents. This indicated that the electron beam-induced damage of the TiO_2 support is compensated by the gas species in the sample vicinity. Ionized gas species might act as oxygen donor to the support. The authors showed that both the current density of the beam and the total dose of the high-energetic electrons have to be taken into consideration when designing the experiment.

3.4 Conclusion and Outlook

The interactions between the electron beam and the gas surrounding the sample results in a non-negligible effect on the microscope performance. The more pronounced effects are the loss of intensity and loss of resolution with increasing pressure, increasing atom-number of the gas, and decreasing acceleration voltage of the microscope. However, by getting a better insight in the physics behind the gas–electron scattering and the contribution to the resulting electron microscope image, quantitative ETEM might be obtainable.

The conventional approached for gaining three-dimensional information of the materials in the TEM, such as electron tomography, is usually not possible in ETEM dynamical ETEM experiments due to the relative long acquisition time. However by relating the intensities and contrast of single images to the sample geometry as demonstrated by Jia et al. (2014) in conventional aberration corrected electron microscopy will add significantly to the dynamic studies where tomography is not an option. In order to adapt the single-shot three-dimensional imaging a full understanding of the imaging process is required, including the electron–gas interactions occurring throughout the microscope column.

Furthermore, the increased reactivity of ionized gases has to be taken into account. A good practise when performing ETEM experiments is to study the influence on beam current density and total dose on the observations and ideally compare with complementary non-electron beam based techniques.

References

P.M. Ajayan, L.D. Marks, Experimental-evidence for quasimelting in small particles. Phys. Rev. Lett. **63**(3), 279–282 (1989)

R. Belkorissat, A.E.D. Kadoun, M. Dupeyrat, B. Khelifa, C. Mathieu, Direct measurement of electron beam scattering in the low vacuum SEM. Microchimica Acta **147**(3), 135–139 (2004). doi:10.1007/s00604-004-0182-x

M.J. Berger, J.S. Coursey, M.A. Zucker, J. Chang, *ESTAR, PSTAR, and ASTAR: Computer Programs for Calculating Stopping-Power and Range Tables for Electrons, Protons, and*

Helium Ions (version 1.2.3) (National Institute of Standards and Technology, Gaithersburg, 2005)

A.N. Bright, K. Yoshida, N. Tanaka, Influence of total beam current on HRTEM image resolution in differentially pumped ETEM with nitrogen gas. Ultramicroscopy **124**, 46–51 (2013). doi:10.1016/j.ultramic.2012.08.007

M. Cabié, S. Giorgio, C.R. Henry, M.R. Axet, K. Philippot, B. Chaudret, Direct observation of the reversible changes of the morphology of Pt nanoparticles under gas environment. J. Phys. Chem. C **114**(5), 2160–2163 (2010). doi:10.1021/jp906721g

F. Cavalca, A.B. Laursen, B. Kardynal, R.E. Dunin-Borkowski, S. Dahl, J.B. Wagner, T.W. Hansen, F. Cavalca, A.B. Laursen, B. Kardynal, R.E. Dunin-Borkowski, S. Dahl, J.B. Wagner, T.W. Hansen, In situ transmission electron microscopy of light-induced photocatalytic reactions. Nanotechnology **23**(7), 075705 (2012). doi:10.1088/0957-4484/23/7/075705

F. Cavalca, A.B. Laursen, J.B. Wagner, C.D. Damsgaard, I. Chorkendorff, T.W. Hansen, Light-induced reduction of cuprous oxide in an environmental transmission electron microscope. Chemcatchem **5**(9), 2667–2672 (2013)

P.M.F.J. Costa, T.W. Hansen, J.B. Wagner, R.E. Dunin-Borkowski, Imaging the oxidation of ZnS encapsulated in carbon nanotubes. Chem. Eur. J **16**(39), 11809–11812 (2010). doi:10.1002/chem.201001301

J.F. Creemer, S. Helveg, G.H. Hoveling, S. Ullmann, A.M. Molenbroek, P.M. Sarro, H.W. Zandbergen, Atomic-scale electron microscopy at ambient pressure. Ultramicroscopy **108**(9), 993–998 (2008). doi:10.1016/j.ultramic.2008.04.014

G.D. Danilatos, *Foundations of Environmental Scanning Electron Microscopy*. Advances in Electronics and Electron Physics, vol. 71 (Academic Press, Boston, 1988), pp. 109–250

G. Danilatos, J. Rattenberger, V. Dracopoulos, Beam transfer characteristics of a commercial environmental SEM and a low vacuum SEM. J. Microsc. **242**(2), 166–180 (2011). doi:10.1111/j.1365-2818.2010.03455.x

A.T. DeLaRiva, T.W. Hansen, S.R. Challa, A.K. Datye, In situ transmission electron microscopy of catalyst sintering. J. Catal. **308**, 291–305 (2013). doi:10.1016/j.jcat.2013.08.018

L.D.L. Duchstein, C.D. Damsgaard, T.W. Hansen, J.B. Wagner, Low-pressure ETEM studies of Au assisted MgO nanorod growth. J. Phys. Conf. Ser. **522**, 012010 (2014). doi:10.1088/1742-6596/522/1/012010

R.F. Egerton, *Electron Energy-Loss Spectroscopy in the Electron Microscope*, 2nd edn. (Plenum Press, New York, 1996)

R.F. Egerton, R. McLeod, F. Wang, M. Malac, Basic questions related to electron-induced sputtering in the TEM. Ultramicroscopy **110**(8), 991–997 (2010). doi:10.1016/j.ultramic.2009.11.003

I.Y. Fugol, V.N. Samovaro, M.G. Starkov, Electron-ion recombination and diffusion in a cryogenic helium plasma. Sov. Phys. JETP USSR **33**(5), 887 (1971)

M. Gajdardziska-Josifovska, R. Sharma, Interaction of oxide surfaces with water: Environmental transmission electron microscopy of MgO hydroxylation. Microsc. Microanal. **11**(6), 524–533 (2005). doi:10.1017/s1431927605050403

P.L. Hansen, J.B. Wagner, S. Helveg, J.R. Rostrup-Nielsen, B.S. Clausen, H. Topsoe, Atom-resolved imaging of dynamic shape changes in supported copper nanocrystals. Science **295** (5562), 2053–2055 (2002). doi:10.1126/science.1069325

T.W. Hansen, J.B. Wagner, R.E. Dunin-Borkowski, T.W. Hansen, J.B. Wagner, R.E. Dunin-Borkowski, Aberration corrected and monochromated environmental transmission electron microscopy: challenges and prospects for materials science. Mater. Sci. Technol. **26**(11), 1338–1344 (2010). doi:10.1179/026708310X12756557336355

T.W. Hansen, J.B. Wagner, T.W. Hansen, J.B. Wagner, Environmental transmission electron microscopy in an aberration-corrected environment. Microsc. Microanal. **18**(4), 684–690 (2012). doi:10.1017/S1431927612000293

T.W. Hansen, A.T. Delariva, S.R. Challa, A.K. Datye, Sintering of catalytic nanoparticles: particle migration or Ostwald ripening? Acc. Chem. Res **46**(8), 1720–1730 (2013)

Q. Jeangros, A. Faes, J.B. Wagner, T.W. Hansen, U. Aschauer, J. Van Herle, A. Hessler-Wyser, R.E. Dunin-Borkowski, In situ redox cycle of a nickel-YSZ fuel cell anode in an environmental transmission electron microscope. Acta Mater. **58**(14), 4578–4589 (2010). doi:10.1016/j.actamat.2010.04.019

C.L. Jia, S.B. Mi, J. Barthel, D.W. Wang, R.E. Dunin-Borkowski, K.W. Urban, A. Thust, Determination of the 3D shape of a nanoscale crystal with atomic resolution from a single image. Nat. Mater. (2014). doi:10.1038/nmat4087

J.R. Jinschek, S. Helveg, Image resolution and sensitivity in an environmental transmission electron microscope. Micron **43**(11), 1156–1168 (2012)

S. Kodambaka, J. Tersoff, M.C. Reuter, F.M. Ross, Germanium nanowire growth below the eutectic temperature. Science **316**(5825), 729–732 (2007). doi:10.1126/science.1139105

T. Kizuka, Formation and structural evolution of magnesium oxide clusters under electron irradiation. Jpn. J. Appl. Phys. Pt. 2: Lett **40**(10A) (2001)

Y. Kuwauchi, H. Yoshida, T. Akita, M. Haruta, S. Takeda, Intrinsic catalytic structure of gold nanoparticles supported on TiO_2. Angew. Chem. Int. Ed. Engl. **124**(31), 7849–7853 (2012)

F. Lenz, Zur Streuung Mittelschneller Elektronen in Kleinste Winkel. Z. Naturforsch. A **9**(3), 185–204 (1954)

P. Li, J. Liu, N. Nag, P.A. Crozier, In situ preparation of Ni–Cu/TiO_2 bimetallic catalysts. J. Catal. 262(1):73–82 (2009). doi:http://dx.doi.org/10.1016/j.jcat.2008.12.001

O. Mansour, K. Aidaoui, A.E.D. Kadoun, L. Khouchaf, C. Mathieu, Monte Carlo simulation of the electron beam scattering under gas mixtures environment in an HPSEM at low energy. Vacuum **84**(4), 458–463 (2009). doi:10.1016/j.vacuum.2009.09.004

O. Mansour, A. Kadoun, L. Khouchaf, C. Mathieu, Monte Carlo simulation of the electron beam scattering under water vapor environment at low energy. Vacuum **87**, 11–15 (2013). doi:10.1016/j.vacuum.2012.06.006

M. Sidorov (2003). http://www.maxsidorov.com/ctfexplorer/

A.G. Nasibulin, L. Sun, S. Hämäläinen, S.D. Shandakov, F. Banhart, E.I. Kauppinen, In situ TEM observation of MgO nanorod growth. Crystal Growth Des. **10**(1), 414–417 (2010). doi:10.1021/cg9010168

L.-M. Peng, S.L. Dudarev, M.J. Wheelan, *High-Energy Electron Diffraction and Microscopy* (Oxford University Press, Oxford, 2004)

F.M. Ross, J. Tersoff, M.C. Reuter, Sawtooth faceting in silicon nanowires. Phys. Rev. Lett. **95** (14), 146104 (2005). doi:10.1103/PhysRevLett.95.146104

S. Janbroers, P.A. Crozier, H.W. Zandbergen, P.J. Kooyman, A model study on the carburization process of iron-based Fischer–Tropsch catalysts using in situ TEM–EELS. Appl. Catal. B. 102 (3–4):521-527(2011). doi:http://dx.doi.org/10.1016/j.apcatb.2010.12.034

R. Sharma, Kinetic measurements from in situ TEM observations. Microsc. Res. Tech. **72**(3), 144–152 (2009). doi:10.1002/jemt.20667

S.B. Simonsen, I. Chorkendorff, S. Dahl, M. Skoglundh, J. Sehested, S. Helveg, Direct observations of oxygen-induced platinum nanoparticle ripening studied by in situ TEM. J. Am. Chem. Soc. **132**(23), 7968–7975 (2010). doi:10.1021/Ja910094r

B.W. Smith, D.E. Luzzi, Electron irradiation effects in single wall carbon nanotubes. J Appl Phys **90**(7), 3509–3515 (2001). doi:10.1063/1.1383020

D.S. Su, M. Wieske, E. Beckmann, A. Blume, G. Mestl, R. Schlögl, Electron beam induced reduction of V_2O_5 studied by analytical electron microscopy. Catal. Lett. **75**(Part 1/2), 81–86 (2001)

M. Suzuki, T. Yaguchi, X.F. Zhang, High-resolution environmental transmission electron microscopy: modeling and experimental verification. Microscopy **62**(4), 437–450 (2013). doi:10.1093/jmicro/dft001

W.F. van Dorp, I. Lazic, A. Beyer, A. Gölzhäuser, J.B. Wagner, T.W. Hansen, C.W. Hagen, W.F. van Dorp, I. Lazic, A. Beyer, A. Gölzhäuser, J.B. Wagner, T.W. Hansen, C.W. Hagen,

Ultrahigh resolution focused electron beam induced processing: the effect of substrate thickness. Nanotechnology **22**(11), 115303 (2011). doi:10.1088/0957-4484/22/11/115303

S.B. Vendelbo, P.J. Kooyman, J.F. Creemer, B. Morana, L. Mele, P. Dona, B.J. Nelissen, S. Helveg, Method for local temperature measurement in a nanoreactor for in situ high-resolution electron microscopy. Ultramicroscopy **133**, 72–79 (2013). doi:10.1016/j.ultramic.2013.04.004

S.B. Vendelbo, C.F. Elkjaer, H. Falsig, I. Puspitasari, P. Dona, L. Mele, B. Morana, B.J. Nelissen, R. van Rijn, J.F. Creemer, P.J. Kooyman, S. Helveg, Visualization of oscillatory behaviour of Pt nanoparticles catalysing CO oxidation. Nat. Mater. **13**(9), 884–890 (2014). doi:10.1038/NMAT4033

J.B. Wagner, F. Cavalca, C.D. Damsgaard, L.D.L. Duchstein, T.W. Hansen, Exploring the environmental transmission electron microscope. Micron **43**(11), 1169–1175 (2012). doi:10.1016/j.micron.2012.02.008

D. Wang, D.S. Su, R. Schlögl, Electron beam induced transformation of MoO_3 to MoO_2 and a new phase MoO. Z. Anorg. Allg. Chem **630**(7), 1007–1014 (2004). doi:10.1002/zaac.200400052

T. Yaguchi, M. Suzuki, A. Watabe, Y. Nagakubo, K. Ueda, T. Kamino, Development of a high temperature-atmospheric pressure environmental cell for high-resolution TEM. J. Electron Microsc. (Tokyo) **60**(3), 217–225 (2011). doi:10.1093/jmicro/dfr011

G.W. Zhou, L. Wang, R. Birtcher, P. Baldo, J. Pearson, J. Yang, J. Eastman, Cu_2O island shape transition during Cu-Au alloy oxidation. Phys. Rev. Lett. **96**(22), 226108 (2006). doi:10.1103/PhysRevLett.96.226108

G. Zhou, L. Luo, L. Li, J. Ciston, E.A. Stach, J.C. Yang, Step-edge-induced oxide growth during the oxidation of Cu surfaces. Phys. Rev. Lett. **109**(23), 235502 (2012). doi:10.1103/PhysRevLett.109.235502